Materials Advances

ROYAL SOCIETY OF CHEMISTRY

PAPER

View Article Online
View Journal | View Issue

Cite this: *Mater. Adv.*, 2025, **6**, 1679

An NIR-luminescent nitrate-bridged hybrid bimetal dielectric with a switchable dielectric constant†

Li-Ping Wang,[a] Lu-Lu Jiang,[a] Zong-Ze Cui,[a] Zheng-Hui Hu,[b] Le-Ping Miao,[a] Jian-Rong Li,*[a] Heng-Yun Ye*[a] and Chao Shi*[a]

Received 8th December 2024,
Accepted 21st January 2025

DOI: 10.1039/d4ma01208a

rsc.li/materials-advances

Hybrid perovskites are highly desirable for potential applicationsin optoelectronics. Although luminescent hybrid perovskites have a variety of technically important applications, achieving dielectric transition and near-infrared (NIR) luminescence properties simultaneously is still challenging. Herein, utilizing the NIR-luminescent properties of rare-earth ions, an Nd^{3+}-containing nitrate-bridged hybrid bimetal dielectric, $(MQ)_5[K_2Nd_2(NO_3)_{13}]$ (**1**; MQ = *N*-methylquinuclidinium cation), was successfully constructed. It exhibited a switchable dielectric constant (ε') between low- and high-dielectric states along with NIR-luminescent property. The $\varepsilon'_{max}/\varepsilon'_{min}$ contrast was strikingly reached 1.88, and the ε'_{max} was 1.18 times higher than that of silicon nitride. Furthermore, the reversibility of the switchable dielectric constant between the ε'_{max} and ε'_{min} at 1 MHz was observed after many ε'-switching cycles with no obvious weakening, which endowed this material with the desirable thermodynamic stability. Notably, **1** exhibited NIR photoluminescence at 1068 nm with a fluorescence lifetime of 1.920 μs, and the Nd^{3+} ion acted as an activator of the NIR luminescence. This finding represents a significant step toward advanced NIR-emissive responsive dielectrics for optoelectronic applications.

Introduction

Stimuli-responsive materials have been extensively investigated for basic scientific concerns. As a class of modern materials, they display switchable physical properties and have potential applications in thermal, electronic and optical industries.[1] Responsive dielectrics with switchable dielectric constant combined with luminescence properties have been mainly focused on rare-earth-doped inorganic perovskites.[2–5] This is mainly owing to the following two considerations: (i) perovskite structures can easily induce striking amphidynamic features and a switchable dielectric constant; (ii) rare-earth ions possess unique optical properties that allow them to emit light in wide spectral ranges (from ultraviolet, visible to near-infrared).[6,7] The optoelectronic materials combining switchable dielectric constant with luminescence properties can be used in rewritable information storage, data communication, and photoelectric devices, among others.[8–11] However, the research on combining optoelectronic materials with switchable dielectric constant and luminescence properties is limited owing to the inherent structural rigidity, and their structural diversity and tunability are still a challenge.

In recent years, hybrid perovskites have shown great advantages in realizing soft multifunctional stimuli-responsive materials.[12–15] The use of organic groups increases their flexibility in molecular design and adaptability in different fields, which greatly expands the application scope of stimuli-responsive materials. For example, Mn^{2+}- and/or Cd^{2+}-containing hybrid multifunctional stimuli-responsive materials exhibit a prominent change of electric permittivity and strong photoluminescence.[16] In addition, luminescent rare-earth materials are an important part of the luminescent field. RE^{3+}-containing responsive dielectrics showing excellent luminescence efficiency and thermal stability have also been characterized and reported. Furthermore, a breakthrough in the realization of rare-earth luminescence hybrid dielectrics with switchable dielectric constant has been very recently made by the synthesis of hybrid double perovskites containing Ce^{3+}, Pr^{3+}, Sm^{3+}, Eu^{3+}, or Dy^{3+}.[17] These smart materials exhibit light emission within a wide range. Accordingly, the RE^{3+}-containing hybrid double perovskites possessing tunable structural characteristics and switchable optoelectronic properties make them promising for next-generation multifunctional materials.

Based on previous works, our follow-up work is continued to screen and further optimize the hybrid rare-earth double

[a] *Chaotic Matter Science Research Centre, International Institute for Innovation, Jiangxi University of Science and Technology, Nanchang 330000, Jiangxi Province, P. R. China. E-mail: jrli@fjirsm.ac.cn, yehy@seu.edu.cn, 13064147687@163.com*
[b] *Anhui Provincical Key Laboratory for Degradation and Monitoring of Pollution of the Environment, School of Chemistry and Materials Engineering, Fuyang Normal University, Fuyang 236037, P. R. China*

† Electronic supplementary information (ESI) available. CCDC 2400883 and 2400884. For ESI and crystallographic data in CIF or other electronic format see DOI: https://doi.org/10.1039/d4ma01208a

perovskite-type amphidynamic materials. Herein, an exploration of the switchable dielectric constant and NIR-luminescent property in an Nd^{3+}-containing nitrate-bridged hybrid bimetal dielectric, $(MQ)_5[K_2Nd_2(NO_3)_{13}]$ (**1**; MQ = *N*-methylquinuclidinium cation), is reported. **1** undergoes reversible structural phase transition-associated bulk property at 175/190 K (cooling/heating, respectively). Various-temperature X-ray diffraction analyses demonstrate that the three-dimensional perovskite structure with the reorientable MQ in the anionic cage guarantees phase transitions. This generates switchable ε' between low- and high-dielectric states due to the motional changes of the molecular dipoles. More importantly, **1** has an NIR-luminescent property, and the Nd^{3+} acts as the activator of the NIR luminescence. This finding is helpful in understanding the origin of the switchable dielectric properties in hybrid rare-earth double perovskites and further exploration of the optoelectronic properties in the future. Here, we report the preparation, variable-temperature single-crystal structures, switchable dielectric constants and NIR-luminescent properties of **1**.

Experimental section

Synthesis

All chemicals are commercially available from Aladdin and were directly used without further purification.

Synthesis of (MQ)I. Quinuclidine (0.556 g, 5 mmol) and CH_3I (0.852 g, 6 mmol) were added in 50 mL ethyl acetate and stirred at room temperature. After the reaction for 24 hours, a large amount of white powder was formed, which was filtered. A powdered (MQ)I was obtained by drying at 333 K for 30 minutes. Yield: 1.20 g, 85.1%, based on quinuclidine.

Synthesis of crystalline 1. In order to eliminate the interference of iodide ions on the reaction system, the as-synthesized of (MQ)I (1.265 g, 5 mmol) was firstly reacted with 1.84 mL of HNO_3 (68%, aq., 10 mmol) at room temperature; iodide ion was oxidized to elemental iodine. Elemental iodine was removed by heating to 363 K until the solution was clear and transparent. A solution of $(MQ)NO_3$ was obtained, named solution A. Then, $Nd(NO_3)_3{\cdot}6H_2O$ (0.877 g, 2 mmol), KCl (0.149 g, 2 mmol) and 0.92 mL HNO_3 (68%, aq., 5 mmol) were added to 25 mL deionized water, stirred and dissolved to form solution B. The mixture of solution A and solution B was stirred, and finally, 10 mL of deionized water was added to reduce the crystal precipitation rate and improve the crystal quality. The mixture was filtered and placed on a heating stage of 313 K to volatilize the solvent, and light purple single crystals were formed in about 2–3 days, which were then collected and dried to obtain $(MQ)_5[K_2Nd_2(NO_3)_{13}]$ with a yield of 71.8% based on the $Nd(NO_3)_3{\cdot}6H_2O$.

The element analysis for 1. Anal. (%) calc.: C 26.64, H 4.46, N 13.99. Found (%): C 26.60, H 4.51, N 13.94 (Table S1, ESI†).

Physical property characterization

Differential scanning calorimetry (DSC) measurements were carried out on a DSC 214 Polyma instrument from 135 K to 240 K at a scanning rate of 20 K min^{-1} under nitrogen. The powder X-ray diffraction (PXRD) patterns were collected on a Rigaku SmartLab X-ray diffraction instrument in the 2θ range from 5° to 50° at room temperature. A Rigaku synergy diffractometer was utilized for temperature X-ray diffraction analyses, which collected data using Mo-K_α radiation (λ = 0.71073 Å) and a graphite monochromator. The pressed-powder pellet with a thickness of about 0.8 mm and an area of about 4 mm^2 was used for dielectric constant measurements. The parallel copper electrodes were formed using carbon glue coated on the surface of the pellet. Variable-temperature dielectric constant (ε') spectra were obtained using the Tonghui TH2828A impedance analyzer in the frequency range of 0.5–1 MHz under an applied electric field of 1.0 V. The UV absorption spectroscopy was performed on a Shimadzu UV-3600i Plus instrument, Japan, with a measurement range of 200–800 nm. Steady-state PL emission and PL excitation (PLE) spectra were collected using a PL spectrometer (FLS980; Edinburgh Instruments). Temperature-dependent steady-state and TRPL spectra were recorded using an FLS980 spectrometer (Edinburgh) equipped with an 800 nm picosecond pulsed laser. FT-IR data of **1** was collected on an FT-IR absorption spectrometer model Thermo Nicolet iS5 (Fig. S1, ESI†) with a frequency range of 4000 to 500 cm^{-1}.

Results and discussion

Thermal properties

The light purple block-like crystal of **1** was obtained by slowly evaporating the aqueous solution on a heating table (Fig. S2, ESI†). The purity of **1** was confirmed by powder X-ray diffraction (PXRD) (Fig. 1a). Meanwhile, the measurement of differential scanning calorimetry (DSC) was performed on **1** to verify the reversible phase transition behavior triggered by temperature. In the measured temperature range of 135–240 K, the DSC curve shows a pair of peak anomalies upon cooling at around 175 K and upon heating at around 190 K, suggesting a phase transition in the temperature range (Fig. 1b). The step-like peak shape and the relatively large thermal hysteresis indicate the character of the first-order transition. The phase transition is accompanied by relatively large enthalpy change (ΔH) of 4535.9 kJ mol^{-1}, and entropy change (ΔS) of 24.8 J mol^{-1} K^{-1}. From the Boltzmann equation $\Delta S = R{\cdot}\ln N$ (where R is the gas constant), the value of N was calculated to be about 19.9, which is moderate among the recent emerging hybrid dielectrics. The value also indicates that the phase transition is of the order–disorder type.

Crystal structures

In order to investigate the mechanism of reversible structural phase transition, X-ray single crystal diffraction experiments were measured at 153 K and 300 K. At 153 K, **1** belongs to the monoclinic space group $P2_1/n$, and the cell parameters a = 16.9414(4) Å, b = 19.8856(4) Å, c = 20.5129(4) Å and β = 93.6825(18)° (Table S2, ESI†). **1** is a nitrate-bridged hybrid bimetal perovskite with a three-dimensional structure with the

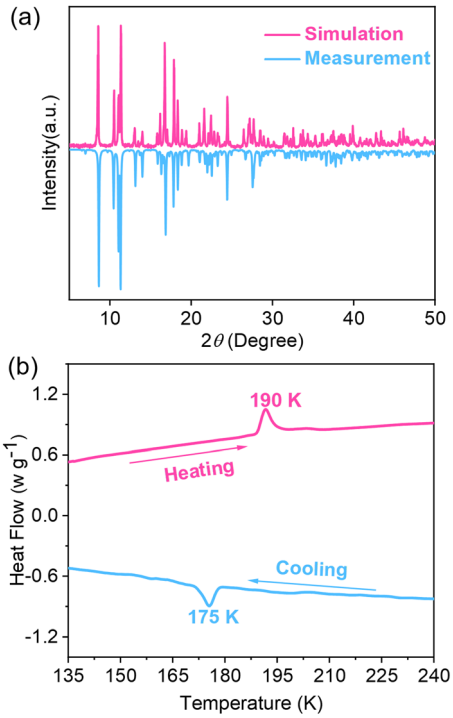

Fig. 1 (a) PXRD pattern for **1** measured at room temperature. (b) DSC curves of **1** measured in a cooling-heating cycle with a rate of 20 K min^{-1}.

simplified formula $A_{2.5}B^{I}B^{III}X_{6.5}$, which differs from the common $A_2B^{I}B^{III}X_6$ (Fig. 2a). The basic asymmetric unit consists of two interesting hexagonal rings to form an anionic framework, where the $Nd(NO_3)_6$ anions are the common part and eight MQs are located within the framework in which they exist in an ordered state (Fig. 2b). The two rings are divided into A-ring and B-ring. The A-ring contains four $Nd(NO_3)_6$, four $K(NO_3)(O_5)$, and two $K(O_6)$ anions, and the structure is approximately centrosymmetric (Fig. 2c). $K(NO_3)(O_5)$ and $K(O_6)$ anions located at the right-upper corner of the A-ring are chelated to the three O atoms from $Nd(NO_3)_6$ unit to form a μ_2-κ^3(O,O′) bridge. It is found that unconventional bridging methods are the root of structural specificity. In contrast, the difference between the B-ring and the A-ring is that the $K(NO_3)(O_5)$ anion is replaced by the $K(O_6)$ anion (Fig. 2d).

At 300 K, **1** crystallizes in the monoclinic space group $P2/m$ with cell parameters of a = 13.0202(5) Å, b = 9.9730(3) Å, c = 13.9707(5) Å and β = 101.914(4)° (Table S2, ESI†). As shown in Fig. 3a and b, except for the two MQ cations in the anion framework, the other six cations show disordered states, and the cation dispersion is more orderly, which is caused by the regional free volume of the anion cage and the weak intermolecular interaction between the cation and the anion cage. It undergoes a drastic structure change. The MQs and NO_3^- show a completely two-site disordered state (Fig. 3c and d). Furthermore, the highly distorted version of the nitrate-bridged hybrid bimetal perovskite structure is characterized by the tilting distortions of the anion framework. In the A-ring, the angles of the Nd–K_{NO_3}–Nd are 121.224° and 120.527°; Nd–K_{NO_3}–K are 98.988° and 97.496°; meanwhile, the angles of the Nd–K–K_{NO_3}

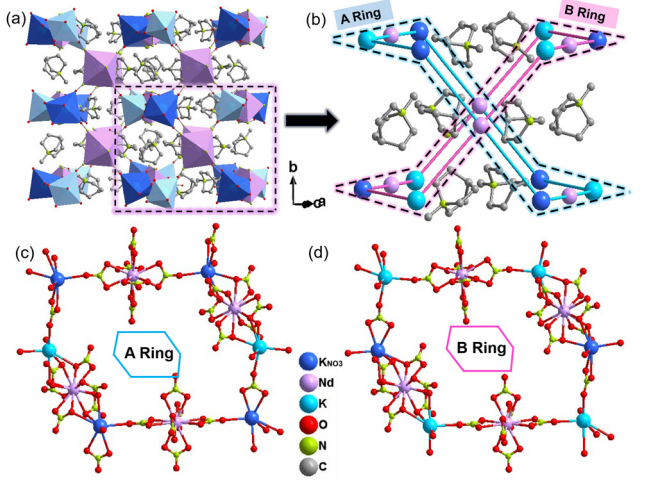

Fig. 2 (a) Packing structures of **1** at 153 K. (b) Simple diagram of the bicyclic crystal structure at 153 K. Note: the ligands of metal atoms are omitted. (c) Structure of A-ring at 153 K. (d) Structure of B-ring at 153 K. Note: K_{NO_3} stands for K atom with NO_3^- coordination. H atoms are omitted for clarity.

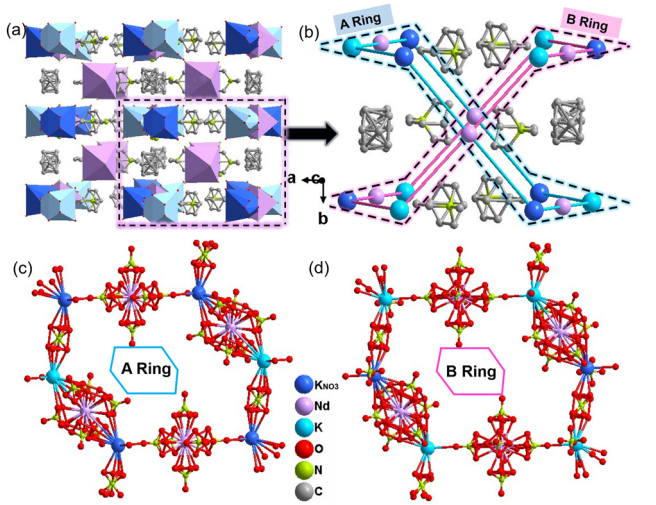

Fig. 3 (a) Packing structures of **1** at 300 K. (b) Simple diagram of the bicyclic crystal structure at 300 K. Note: the ligands of metal atoms are omitted. (c) Structure of A-ring at 300 K. (d) Structure of B-ring at 300 K. Note: K_{NO_3} stands for K atom with NO_3^- coordination. H atoms are omitted for clarity.

are 124.212° and 119.467° at 153 K, respectively. The result shows that the A-ring is slightly rugged. When the temperature increases to 300 K, the angle of the Nd–K_{NO_3}–Nd are transformed into 119.112° and that of Nd–K_{NO_3}–K is transformed into 98.317°. The angle of the Nd–K–Nd is equal to 123.477°. Notably, the B-ring undergoes a similar structural change to the A-ring. Although there is a significant difference between the corresponding angles in the A and B rings at 153 K, the values are the same at 300 K (Fig. S3 and Table S3, ESI†). Various-temperature single-crystal structural analysis revealed the order–disorder transition of the MQs and the motion of the anionic cage-like framework, are attributed to the phase transition.

Dielectric measurements

The switchable property of **1** was revealed by the T–ε' measurement. The powdered sample of **1** was investigated within the temperature range from 130 K to 220 K and the frequency ranges of 0.5–1 MHz (Fig. 4a). **1** shows the striking dielectric transition between low and high states, corresponding to the order–disorder structural phase transition. At 1 MHz, the initial dielectric constant of **1** is about 5. In the heating process, the ε' value grows steadily and reaches the peak value of 8.25 at around 190 K due to the phase transition, then keeps relatively flat upon further heating. Upon cooling, the ε' curve is similar to that of the heating mode and exhibits a hysteresis of 15 K of dielectric anomalies, well consistent with the DSC results (Fig. S4, ESI†). The sharp switching of the dielectric constant can be ascribed to the contribution of the orientational polarization of the MQs. This type of dynamic change has been extensively investigated in the hybrid perovskite. Furthermore, this ε' switch "ON → OFF" corresponds well to the switchable dielectric constant from a low-dielectric state (LDS) to a high-dielectric state (HDS). It can be seen that the ε' curves upon heating–cooling cycles manifest quite a similarity, further revealing its reversible characteristic. Notably, the excellent reversibility of **1** was also observed after many ε'-switching cycles with no obvious decay, which endows this new hybrid bimetal dielectric with desirable stability (Fig. 4b).

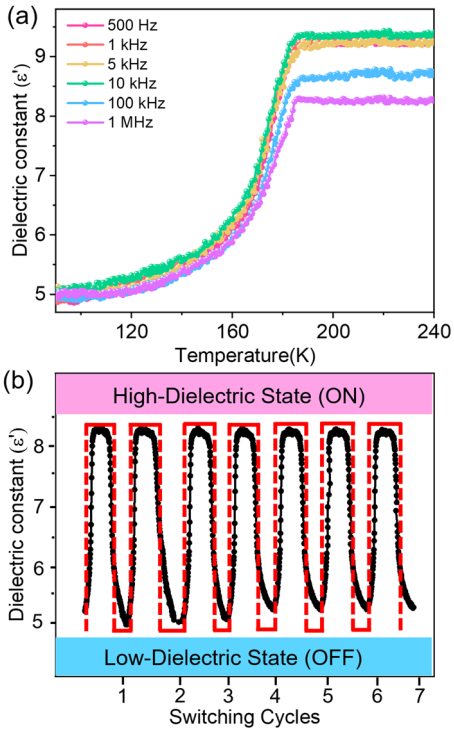

Fig. 4 (a) Switchable T–ε' curves of **1** measured in the range from 500 Hz to 1 MHz (in the heating process). (b) ε'-switching cycles of **1** determined at 1 MHz. The dielectric property of **1** was obtained using a polycrystalline sample.

Fluorescence properties

Furthermore, **1** also has NIR photoluminescent properties attributed to an electronic transition (also known as an f–f transition) of the 4f shell of Nd^{3+}. The absorption spectrum is illustrated in Fig. 5a, and the assignment of the electron transitions of those typical peaks is included. In the absorption spectrum, the absorption bands are the same as those for the starting material $Nd(NO_3)_3{\cdot}6H_2O$ (Fig. S5, ESI†). The bands above 400 nm are typical for the f → f transitions of the Nd^{3+} ion, while the bands below 400 nm are derived from the absorption of nitrate ligands. The peaks corresponding to the absorption peaks are obtained from the excitation spectrum (λ_{em} = 1066 nm). The excitation peak at 597 nm is the strongest, corresponding to the $^4I_{9/2} \rightarrow {}^4G_{5/2}$ absorption transition (Fig. 5c). In the emission spectrum, there are three main peaks, and the intensity of the $^4F_{3/2} \rightarrow {}^4I_{11/2}$ transition is the strongest. According to the selection rule, the strongest transition is the induced electric dipole transition. From the UV-vis diffuse reflectance spectrum, it can be clearly seen that the highest absorption peak is at 576 nm. According to the temperature dependence of the luminescence spectrum (λ_{ex} = 808 nm), the intensity of fluorescence and the emission spectrum hardly changed (Fig. S6, ESI†), showing anti-thermal quenching performance at low temperatures (Fig. S6, ESI†). The abrupt absorption band edge indicates an indirect bandgap. The optical band gap of **1** was determined by the variant Tauc equation,[18] which is expressed as

$$[(h\nu \cdot F(R_\infty))]^{\frac{1}{2}} = A(h\nu - E_g)$$

where h represents the Planck constant, ν means the photon frequency, $F(R_\infty)$ implies the Kubelka–Munk function and A stands for the proportionality constant. The band gap (E_g)

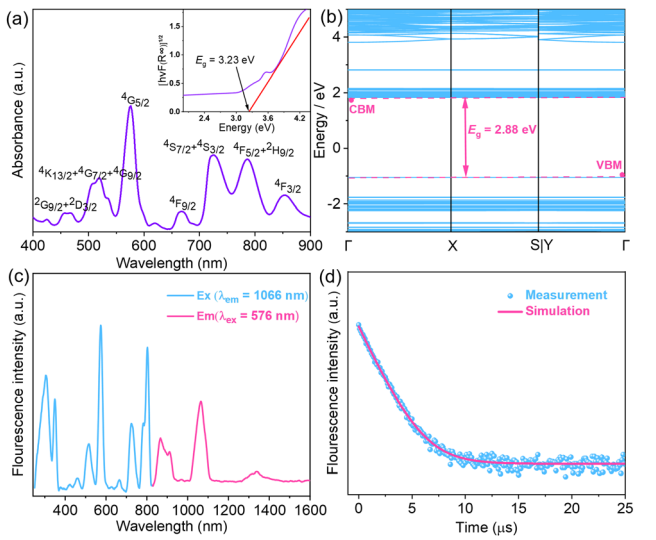

Fig. 5 NIR photoluminescent properties of **1** at room temperature. (a) Absorption spectrum. Embedded map is an absorption spectrum fitting band gap map. (b) The calculated band structure of **1**. (c) Excitation (λ_{em} = 1066 nm) and emission (λ_{ex} = 576 nm) spectra of **1**. (d) Fluorescence decay curve for the $^4F_{3/2} \rightarrow {}^4I_{11/2}$ transition.

of **1** is 3.23 eV (Fig. 5a). Meanwhile, theoretical calculations were performed to confirm the bandgap characteristics (Fig. 5b). The highest point of the valence band (A point) and the lowest point of the conduction band (G point) were observed at different points. The indirect bandgap characteristics of **1** were further verified by theoretical results. In addition, the theoretical calculation value of E_g is 2.88 eV (Note S2, ESI†), which is slightly smaller than the experimental value. More importantly, the value of E_g is moderate among the recently emerging hybrid semiconductors. It would find roles in exploring promising hybrid optoelectronic materials. The fluorescence decay curve of **1** is fitted as a single exponential function:

$$I = A \cdot \exp\left(\frac{-t}{\tau}\right)$$

where I refers to the photoluminescence intensity, A stands for the contrast, t denotes the decay time and τ is related to the decay contrast. The fluorescence lifetime of **1** was calculated to be 1.920 μs (Fig. 5d). The fluorescence lifetime of **1** is improved relative to that of $(R_3HQ)_4[KNd(NO_3)_8]$.[19] The structural symmetry of **1** is improved, the rigid structure is relatively strong and the non-radiative transition is inhibited, thus the fluorescence lifetime is extended.

Conclusions

In conclusion, a three-dimensional Nd^{3+}-containing nitrate-bridged hybrid bimetal dielectric, $(MQ)_5[K_2Nd_2(NO_3)_{13}]$ (**1**; MQ = *N*-methyl quinuclidinium cation), was synthesized. Dynamic changes of the MQs and anion framework generated a typical order–disorder structural phase transition at 175/190 K (cooling/heating, respectively). The switchable dielectric constant made it a new type of dielectric switch. More interestingly, **1** exhibited NIR luminescence property. The Nd^{3+} ion acted as an activator of the NIR luminescence. Furthermore, the optical band gap of **1** was also determined to be about 2.88 eV. However, there is still much room for further studies on structural modifications *via* modifying the rare-earth ion and organic cation. Hybrid bimetal dielectric would drive the exploration of multifunctional smart materials.

Author contributions

C. Shi conceived the project. L.-P. Wang prepared the samples. L.-P. Wang, L.-L. Jing and Z.-Z. Cui performed the dielectric, DSC and PXRD measurements. J.-R. Li and L.-P. Wang measured the emission spectrum and FLT. H.-Y. Ye and L.-P. Miao contributed to single crystal measurement and analysis. C. Shi and J.-R. Li wrote the manuscript, with inputs from all other authors.

Data availability

All data included in this study are available upon request by contacting the corresponding author.

Conflicts of interest

The authors declare no conflict of interest.

Acknowledgements

This work was supported by the National Natural Science Foundation of China (no. 22175079 and 22275075) and the Natural Science Foundation of Jiangxi Province (no. 20225BCJ 23006, 20224ACB204002, and 20204BCJ22015).

Notes and references

1 (*a*) *Handbook of Stimuli-Responsive Materials*, ed. M. W. Urban, Wiley-VCH, Weinheim, 2011; (*b*) P. Theato, B. S. Sumerlin, R. K. O'Reilly and T. H. Epps III, *Chem. Soc. Rev.*, 2013, **42**, 7055–7056; (*c*) S. S. Nagarkar, A. V. Desai and S. K. Ghosh, *Chem. – Asian J.*, 2014, **9**, 2358–2376; (*d*) L. S. Zhang, J. Li, F. Wang, J. D. Shi, W. Chen and X. M. Tao, *Mater. Sci. Eng., R*, 2021, **146**, 100629; (*e*) H. Q. Zheng, L. Zhang, Y. J. Cui and G. D. Qian, *Adv. Photonics*, 2023, **982**, 054001–054005.

2 Q. R. Yao, F. F. Wang, F. Xu, C. M. Leung, T. Wang, Y. X. Tang, X. Ye, Y. Q. Xie, D. Z. Sun and W. Z. Shi, *ACS Appl. Mater. Interfaces.*, 2015, **7**, 5066–5075.

3 (*a*) H. L. Sun, X. Wu, T. H. Chung and K. W. Kwok, *Sci. Rep.*, 2016, **6**, 28677–28684; (*b*) H. L. Sun, X. Wu, D. F. Peng and K. W. Kwok, *ACS Appl. Mater. Interfaces*, 2017, **9**, 34042–34049.

4 D. K. Khatua, A. Kalaskar and R. Ranjan, *Phys. Rev. Lett.*, 2016, **116**, 117601.

5 (*a*) Q. W. Zhang, H. Q. Sun and Y. Zhang, *J. Am. Ceram. Soc.*, 2014, **97**, 868–873; (*b*) H. Q. Sun, Q. W. Zhang and W. X. Li, *Ferroelectrics*, 2016, **490**, 127–135; (*c*) J. C. Qi, Y. Qin, H. Peng, H. P. Lv, Y. J. Bai, X. Shen, Z. T. Xia and W. Q. Liao, *Sci. China Chem.*, 2024, **67**, 4167–4174.

6 S. A. Younis, N. Bhardwaj, S. K. Bhardwaj, K. H. Kim and A. Deep, *Coord. Chem. Rev.*, 2021, **429**, 213620.

7 F. Saraci, V. Quezada-Novoa, P. R. Donnarumma and A. J. Howarth, *Chem. Soc. Rev.*, 2020, **49**, 7949–7977.

8 Y. T. Chen, X. M. Liu, T. F. Wang and Y. X. Zhao, *Acc. Chem. Res.*, 2021, **54**, 3452–3461.

9 H. Wang and D. H. Kim, *Chem. Soc. Rev.*, 2017, **46**, 5204–5236.

10 C. Xie, C. K. Liu, H. L. Loi and F. Yan, *Adv. Funct. Mater.*, 2020, **30**, 1903907–1903934.

11 X. Chen, M. C. Jia, W. Xu, G. C. Pan, J. Y. Zhu, Y. T. Tian, D. Wu, X. J. Li and Z. F. Shi, *Adv. Opt Mater.*, 2023, **11**, 2202153–2202200.

12 (*a*) T. Hang, W. Zhang, H. Y. Ye and R. G. Xiong, *Chem. Soc. Rev.*, 2011, **40**, 3577–3598; (*b*) W. Zhang and R. G. Xiong, *Chem. Rev.*, 2012, **112**, 1163–1195; (*c*) T. Zhang, K. Xu, J. Li, L. He, D. W. Fu, Q. Ye and R. G. Xiong, *Natl. Sci. Rev.*, 2023, **10**, nwac240–nwac257; (*d*) Q. Pan, Z. X. Gu, R. J. Zhou, Z. J. Feng, Y. A. Xiong, T. T. Sha, Y. M. You and R. G. Xiong, *Chem. Soc. Rev.*, 2024, **53**, 5781–5861.

13 W. Li, Z. M. Wang, F. Deschler, S. Gao, R. H. Friend and A. K. Cheetham, *Nat. Rev. Mater.*, 2017, **2**, 16099–16116.

14 (*a*) L. Lu, X. Pan, J. H. Luo and Z. H. Sun, *Chem. – Eur. J.*, 2020, **26**, 16975–16984; (*b*) H. J. Xu, S. G. Han, Z. H. Sun and J. H. Luo, *Acta Chim. Sin.*, 2021, **79**, 23–35; (*c*) Y. Y. Chen, C. H. Gao, T. Yang, W. J. Li, H. J. Xu and Z. H. Sun, *Chin. J. Struct. Chem.*, 2022, **41**, 2204001.

15 (*a*) A. A. Zhumekenov, M. Saidaminov, O. F. Mohammed and O. M. Bakr, *Joule*, 2021, **5**, 2027–2046; (*b*) G. Vats, B. Hodges, A. J. Ferguson, L. M. Wheeler and J. L. Blackburn, *Adv. Mater.*, 2023, **35**, 2205459–2205491; (*c*) A. Kanwat, N. Yantara, P. Kajal and N. Mathews, *Adv. Opt. Mater.*, 2023, **28**, 2301342–2301369.

16 (*a*) Z. X. Zhang, C. Y. Su, J. X. Gao, T. Zhang and D. W. Fu, *Sci. China Mater.*, 2021, **64**, 706–716; (*b*) J. A. Zienkiewicz, D. A. Kowalska, K. Fedoruk, M. Stefanski, A. Pikul and M. Ptak, *J. Mater. Chem. C.*, 2021, **9**, 6841–6851; (*c*) M. Maczka, D. Stefanska, M. Ptak, A. Gagor, A. Pikul and A. Sieradzki, *Dalton Trans.*, 2021, **50**, 2639–2647; (*d*) J. J. Wu, Y. Guo, J. L. Qi, W. D. Yao, S. X. Yu, W. L. Liu and S. P. Guo, *Angew. Chem., Int. Ed.*, 2023, **62**, e202301937; (*e*) Z. L. He, J. H. Wei, J. B. Luo, Z. Z. Zhang and D. B. Kuang, *J. Mater. Chem. C.*, 2023, **11**, 1251–1257.

17 (*a*) M. M. Hua, L. Ye, Q. W. Wang, J. J. Ma, Z. X. Gong, Q. Xu, C. Shi and Y. Zhang, *J. Mater. Chem. C.*, 2020, **8**, 16349–16353; (*b*) M. L. Tarlton, S. Skanthakumar, D. Hutchison, A. J. Gremillion, A. G. Oliver and R. E. Wilson, *Inorg. Chem.*, 2022, **61**, 17101–17108; (*c*) M. L. Tarlton, T. D. Persinger, N. M. Byrne, T. C. Douglas, A. Yakovenko and R. E. Wilson, *Inorg. Chem.*, 2023, **62**, 16770–16781; (*d*) H. K. Li, L. P. Wang, Z. Z. Cui, Q. Xu, L. L. Zou, N. Wang, L. P. Miao, H. Y. Ye and C. Shi, *J. Mater. Chem. C.*, 2024, **12**, 14122–14128; (*e*) Q. H. Zou, Z. J. Wang, L. K. Wu, Y. Feng, L. L. Jiang, J. R. Li, H. Y. Ye and C. Shi, *Inorg. Chem.*, 2024, **63**, 10817–10822; (*f*) H. Xiao, L. Y. Sheng, S. Chen, R. K. Huang, C. H. Zeng, Z. Y. Du, C. T. He, W. X. Zhang and X. M. Chen, *Inorg. Chem. Front.*, 2024, **11**, 5336–5344.

18 J. Tauc, R. Grigorovici and A. Vancu, *Phys. Status Solidi B*, 1966, **15**, 627–637.

19 H. K. Li, L. P. Wang, N. Wang, Z. Z. Cui, L. L. Zou, L. P. Miao, H. Y. Ye and C. Shi, *Chem. Mater.*, 2024, **36**, 8846–8853.